Master Thesis

Improved Range of Motion of a Redundantly Actuated 3-DOF Planar Manipulator with Flexure Joints

Maurice van der Ploeg

Graduation Committee:

Dr.Ir. R.G.K.M. Aarts
Dr.Ir. J.P. Schilder
Dr.Ir. M. Nijenhuis

Mechanical Engineering
Chair of Applied Mechanics and Data Analysis

University of Twente

August 2023

Summary

Flexure based parallel manipulators are well suited mechanisms for precision engineering applications. The advantages are low hysteresis,lack of friction and backlash. Disadvantages of flexible manipulators are that the support stiffness lowers when it is deflected and that the load bearing capacity is limited. The use of a additional redundant arm compensates for these disadvantages. The redundancy adds support stiffness, increases torque delivery to the system and allows for better measurement accuracy.

This study focuses on improving the work range of a redundantly actuated 3-DOF planar manipulator with flexure joints. The redesign is focused on the properties and limitations specific to a parallel manipulator with flexure joints. The redesign process involves a reconsideration of the joints and topology of the system. The chosen configuration is optimized using a multi objective optimization process in MATLAB in order to find the best compromise. This study also provides a kinematic and dynamic analysis of the system with a solution for redundant actuation and sensing. This information can be used in further research to implement the suggested controller.

The found optimum achieves a larger workspace compared to the previous design, However the desired dynamic properties of the system are not reached. A physical model of the system is developed to perform experimental testing in the future.

Acknowledgement

The author of this master thesis would like to express gratitude for the time and expertise that Dr. Ir. Ronald Aarts has provided. His supervision and support resulted in a memorable graduation period.

Contents

1 Introduction

The demand for semiconductors is increasingly growing. However, the production capacity is not able to keep up with the demand. Therefore the need for high precision actuators is expanding rapidly. Flexure mechanisms, also known as compliant mechanisms, provide a well-suited solution in the field of precision engineering. The main advantages are to eliminate backlash, friction and hysteresis. This allows for a high precision and high repeatability of the system. Flexure mechanisms are designed to transmit motion and forces with elastic deformation rather than traditional hinges (for example bearings). To obtain the desired motion and restrain undesired motion, a correct design of the flexure elements is important. One of the challenges of a flexure mechanisms lies in the deformed supporting direction stiffness. The compliance in the supporting direction is a key design parameter for the performance, precision, load-bearing capability and stability of the system. In the desired direction the stiffness needs to be low enough to achieve enough displacement. In all other direction the stiffness is desired to be as high as possible. The work range of a compliant mechanism is often more limited than its conventional counterpart. This is mainly because the movement made possible with elastic deformation is always limited to the maximum allowable stress in the material.

One of the methods found to improve the support stifness in a deformed state of compliant mechanism is to use redundancy [1]. The redundancy adds an additional arm, actuator and encoder. This results in four components instead of three in case of a three degrees of freedom (DOF) system. An additional method is to make use of a Parallel Kinematic Manipulators (PKM) design. This method of desiging only uses actuators in the base of the system. The advantage is that the weight of the actuators do not affect the weight of the manipulator. This is beneficial for the required support stiffness [2]. The use of redundancy in combination with PKM means that the additional actuator will not negatively impact the manipulator. The additional arm and actuator also increase the total torque available in the system, which enables higher accelerations. Another benefit arises from the additional sensor, which allows for redundant sensing, which leads to smaller error. Additionally, redundancy will help in preventing singularities in the workspace [3]. However, the redundancy increases the sensitivity for misalignment and also provides problems for the controlling of the system as multiple solutions are possible [4]. The support stiffness of the compliant mechanism corresponds to the parasitic natural frequencies found in the system. The parasitic frequencies are all eigen-frequencies associated with a vibration mode in the constraint direction. These eigen-freqcuencies, in particular the first parasitic frequencies, have a direct impact on the controller performance. It limits the crossover frequency of the controller, thus affecting the bandwidth and stability of the controller [5]. The dynamics of a compliant mechanism can be modelled thoroughly and is therefore suitable to incorporate in a optimization process. However the dynamic modelling is limited in accuracy for large deformations where non linearities may occur. Due to the design complexity of some manipulators the only viable manufacturing process is 3D-printing.

Previous studies explored the possibilities of a 2 degree of freedom planar manipulator. The first iteration showed the benefits of redundancy, preloading and pre-bending of joints. The resulting design is visible in Figure 1a. These factors contributed to a higher support stiffness throughout the workspace and lowered actuator torques. [1] [6]. The following iteration of the system used the redundantly actuated 2 DOF planar manipulator concept and reconsidered the design philosophy. The redesign of the system focuses on a larger workspace while maintaining a high parasitic eigen-frequency. It also confirmed the advantages of using pre-load to lower the required actuator torque [7] [8]. Another study developed a a 3 degree of freedom redundantly actuated parallel manipulator with flexure hinges. The main focus of this study was to expand from 2 degrees of freedom to 3. In addition it focused on optimizing the mechanical properties of system, specifically the parasitic eigen-frequency [9].

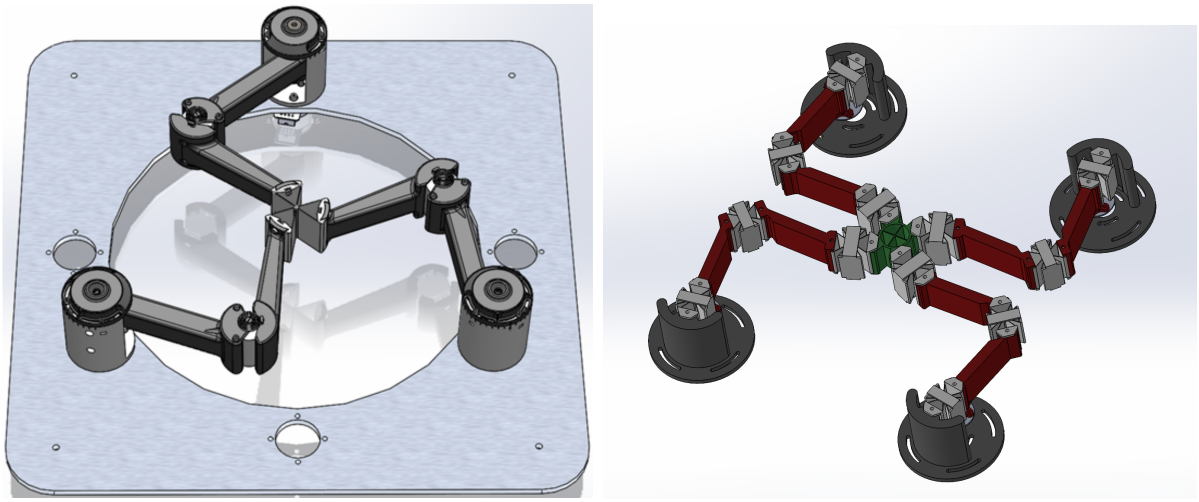

(a) 2DOF manipulator CAD model [7]

(b) 3DOF manipulator CAD model

Figure 1: Evolution of the redundantly actuated planar manipulator with flexure joints

This research will focus on the redesign of a 3DOF redundantly actuated compliant mechanism. The goal is to improve the available workspace. Design parameters have significant impact on the mechanical properties of the system and always lead to a compromise between the workspace size and dynamic properties of the system. In order to find a new design that prioritizes workspace, a multi-objective optimization process is used. For this process first a global system design is obtained using literature and modelling techniques in MATLAB. Consecutively parameters are identified in order to find a set of important parameters that describe the mechanical properties of the system. These parameters are used to fine-tune the design by modelling it in SPACAR and optimizing this model with MATLAB. The design found as an optimum is analysed and finally converted from a theoretical SPACAR model to a 3D auto-cad model in Solidworks. Figure 1b shows the final design presented in this research.

2 Method: Design of the mechanical model

This chapter covers the general design of the system and the different components. Previous research of the redundantly actuated flexure mechanism allows for a starting point for the general system design. As stated before, the main goal is to improve the range of motion of the end-effector. While keeping this goal in mind, there are more aspects that need to be considered to produce a suitable design for a 3DOF parallel manipulator. A detailed overview of these aspects is provided in the following chapters.

2.1 Design requirements

To initiate a design, it is important to establish the specific requirements for which the design is intended. During optimization a compromise between the different requirements will be found. This compromise will inherently lead to a form of subjectivity in prioritizing different requirements. The following requirements are considered for the design:

- A Large workspace in all degrees of freedom
- The stress remains below the tensile strength of the material and only have elastic deformation in the flexure hinges
- Low flexure hinge stiffness in the driven direction. This is in direct relation with the actuator effort needed to move the end-effector
- High flexure hinge stiffness in all support directions. This requirement is necessary for good controller performance and it is important to achieve load-bearing capacity. The expected first parasitic frequency of the whole system is the out of plane mode [9][10][8][1].
- No interference between the different parts of the system. Interference physically limits the maximum workspace and can lead to structural failures.

The design will follow these requirements. In the following subsections the components of the manipulator are introduced with their respective design aspects.

2.2 Topology of the system

The general configuration of the system already establishes some of the mechanical properties. As mentioned before, the system consist of four actuators and arms due to the redundancy. Each of the four actuators is connected to the fixed world and to a arm. Each arm essentially operates as a double pendulum with one hinge connecting the upper and lower arm, another hinge connecting the lower arm to the end effector and a final hinge connecting the upper arm to the fixed world. The definition of these hinges is as follows: the hinge at the actuator position is called the shoulder hinge, the hinge connecting both arms is the elbow hinge and the hinge at the end of the lower arm is the wrist hinge. These definitions are also visible in Figure 2. The end-effector square connects all arms together such that the movements of all actuators combined determine the movement of the end-effector. The degrees of freedom for the end-effector are translation in x and y direction and in-plane rotation.
The end-effector size determines the ability of the actuators to apply torque in the rotational degree of freedom. A large distance from the wrist hinge to the centre of the end-effector results in more torque applied to the rotational degree of freedom for a given actuator torque. The distance between points on the end-effector that connect to the wrist needs to be chosen such that no interference will occur.

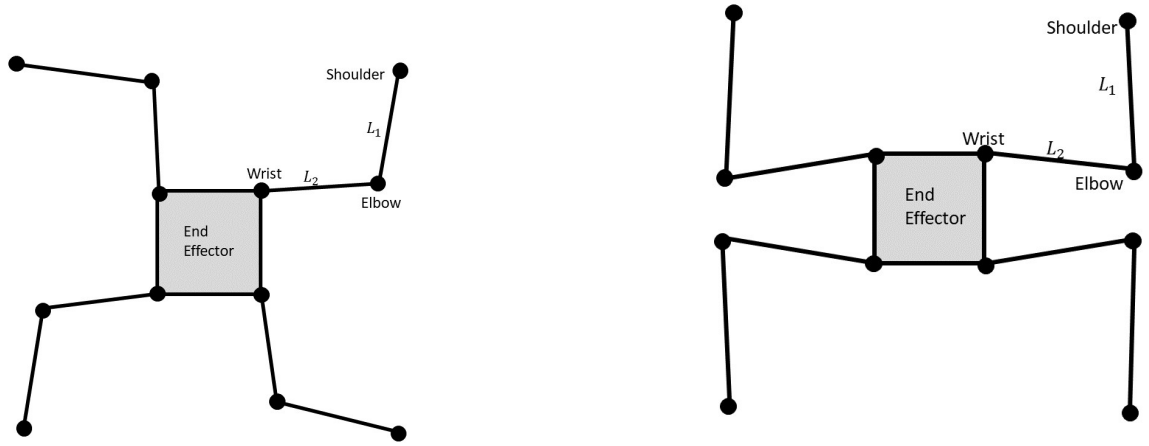

(a) Configuration 4 way symmetry

(b) Configuration 2 way symmetry

Figure 2: Different possible configurations of a 3 DOF redundantly actuated manipulator

The configuration of each arm can also be chosen. Because each arm acts as a double pendulum, there are two possible configurations for the same wrist hinge position. Choosing which of these configurations is used can result in a variation of configurations of the system. A four way symmetry for the arms is possible where every arm uses the same configuration, this can be seen in Figure 2a. An alternative is to use a two way symmetry where a variation in double pendulum solution is used.
The base locations of the actuators acts as a measure to scale the system to a certain size. It also allows for design freedom to place the actuators closer together or evenly spaced apart. This has impact on the workspace available but also in the support stiffness through the entire workspace [11][12][13]. Previous research used an evenly spaced location for the actuators [9]. The configuration and shape of the end-effector, arms, and actuator location can be optimized.

The design of the arm plays an important role in the workspace of the system and the out of plane eigenfrequency. The definitions of L_1 and L_2 refers to the length of the arms. The arm L_1 is defined as the arm connecting the actuator and shoulder hinge to the elbow. Arm L_2 is defined as the arm connecting the elbow to the wrist hinge. The end-effector is schematically drawn as a square of beams in Figure 2. However, for the final design this is redesigned for ease of assembly and weight reduction. The length of both arms is considered to be equal, as this eliminates a variable of the system and according to earlier reserach [14], will result in the maximum workspace.

2.3 Hinge design

The flexure hinge replaces the traditional hinge. The flexure hinge achieves motion due to elastic deformation. The most basic form of a flexure hinge is made by fixing two sides of a relatively short and flat spring to two members. When applying a moment these members can move due to the deformation of the spring. Such a spring acts relatively rigid to bending in its own plane, but is susceptible to lateral forces or twisting moment [15]. By applying two of such springs under an angle of ± 45 °, some of these disadvantages can be mitigated. This basic flexure hinge is called the cross-flexure hinge and is visible in Figure 3, where members 'a' and 'b' are connected with two flat springs 'c' and 'd'. The line 'e' represents the axis of rotation. Such a cross-hinge provides stable rotation with a relatively small rotation angle. Other problems that can arise with flexure hinges are shift of rotation angle at larger deformations, buckling in the

leaf springs and limited load bearing capacity. However, this behaviour depends on the applied forces and the dimensions of the hinge and can be calculated for every case [15][16].

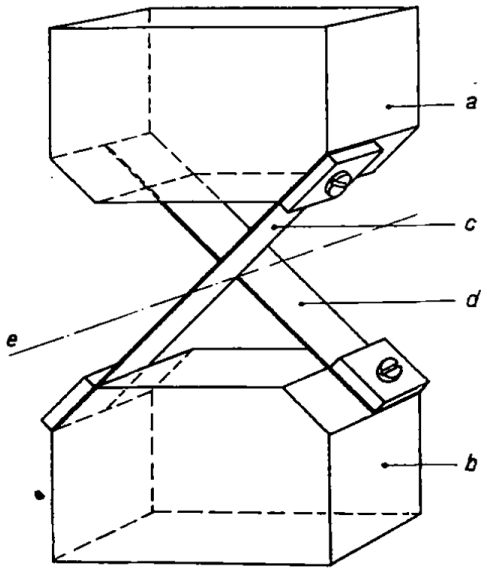

Figure 3: Sketch of a simple cross-spring hinge [15]

In order to create the maximum workspace possible for the system, a large stroke of the hinge is necessary. The difficulty is to maintain support stiffness at these larger deformations. It is generally believed that the butterfly hinge is suitable for a high precision flexure hinge with a large stroke [17]. Another common option is the cartwheel hinge. This is a type of cross hinge where two leaf springs cross in the middle of the hinge and are rigidly connected in the centre point. For the cartwheel and butterfly hinge the definition from earlier research is used [18]. These definitions are shown in Figure 4.

In this Figure the the length of the leaf spring is defined together with an angle α which is set to 45° for a cartwheel hinge. The butterfly hinge essentially uses stacked leaf springs. Research showed that for large stroke butterfly hinges interference between the different element is a limitation. To mitigate this limitation as much as possible the definition for a butterly hinge is used as provided by earlier research [18], this enables to achieve a rotation of ± 30 °. The butterfly hinge is defined with angle $\alpha_1 = 35°$, $\alpha_2 = 55°$, a factor λ and the length L of a individual leaf spring as can be seen in Figure 4b. The definition of the cartwheel hinge and butterfly hinge is similar, which allows for ease of comparison. The angle of 45° is considered to deliver the maximum off-axis stiffness. Therefore the butterfly hinge uses 35° and 55° angles as these values are closest to the 45° optimum while reaching 30° of rotation [18]. A high out off plane stiffness of the hinge is desired to prevent the first parasitic eigen frequency from becoming to low.

2.4 Material selection

The properties of a flexure mechanism can be optimised for using 3D printing technology. The 3D printing allows for fine details, thin leaf springs and intricate design solutions that increase stiffness and reduce weight. The optimal material to use would be a metal with a high allowable stress. Metals can be used to create very thin leaf springs with the possibility for large elastic deformation. However, a 3D metal printing technique results in high production cost. For the goal of this research a prototype needs to be made and with budget constraints general

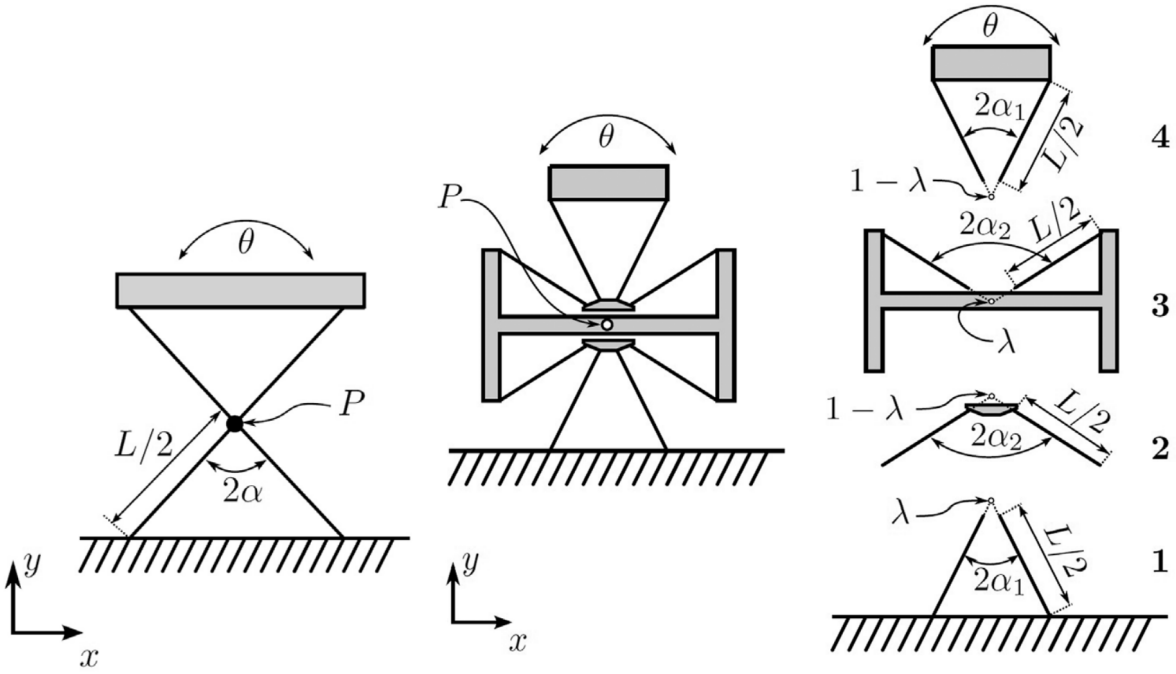

(a) Cartwheel hinge definition [18] (b) Butterfly hinge definition [18]

Figure 4: Overview of the configuration of a Cartwheel and Butterfly hinge

thermoplastic materials are considered. The materials chosen are polylactic acid (PLA) and polyamide (Nylon). PLA is the most economical option and can be used in almost any type of 3D printer. Nylon is compared to PLA a more expensive material but is better suited for fine precision parts. Furthermore, Nylon is well suited for flexure mechanism due to its toughness in bending. PLA on the contrary is a very brittle material. The combination of both Nylon for the flexure hinges and PLA for all other parts is used as a compromise for performance and cost. The material properties are presented in Table 1.

Table 1: Material properties

Material	Property	Value	Unit
PolyLactic Acid (PLA)	Tensile strength	45	[MPa]
	Young's modulus	3.5	[GPa]
	Density	1250	$[\ \mathrm{kg/m^{-3}}]$
Nylon (PA2200) [30]	Tensile strength	45	[MPa]
	Young's modulus	1.7	[GPa]
	Density	930	$[\ \mathrm{kg/m^{-3}}]$

2.5 Motors

The motor available for the test setup is a motor with a high encoder resolution. The encoder measures the angle of the shoulder joint. The angle of the shoulder joint has small angular deformation for a given displacement in the degree of freedom of the end-effector. The high encoder resolution is therefore something that is necessary for a well functioning system. The properties of the motors are given in Table 2. The maximum motor torque is a design parameter. The motor torque dictates the maximum hinge stiffness; with a too high hinge stiffness the motor will not be able to move the end-effector through the whole workspace.

Table 2: Motor properties

Property	Value	Unit
Nominal Torque	0.387	[Nm]
Torque constant	70.5	[mNm/A]
Encoder resolution	25600	[Counts/rev]

2.6 Conclusion design of mechanical model

In the previous design iteration the system was expanded from 2 DOF to 3 DOF and the focus was on improving the out of plane stiffness of the system. In terms op topology, this research [9] found that a four way symmetry of the arms provided the best out of plane stiffness . For the new design the focus is shifted to optimizing the larges workspace. From the perspective of topology and hinge design, the workspace limit is reached either when a hinge reaches its maximum deflection or due to self interference between components.
According to the simulations the topology with a 2 way symmetry over the centre axis allows for a slight advantage in parasitic eigen frequency and allows for larger workspace. This is in line with previous findings [9]. However, this does lead to possible interference between the arms, which can be solved by limiting the maximum length of the arms. The location of each actuator can be varied to mitigate some of this interference and a optimum actuator location can be found. However, simulations showed that the best out of plane stiffness is achieved in the workspace with each actuator equally spaced from each other in a square. The simulations results are given in appendix A. The size of this square is a measure to define the scale of the system. For practical reason the size of the square is equal to previous research. This allows for the reuse of the base plate and will allow for better comparison between the new design and the previous.
Figure 2b shows the topology of the chosen 2 way symmetry system. The choice of hinge design is the butterfly hinge for every hinge location. The main reason is to make use of the large rotational deformation allowed by the butterfly hinge.

3 Dynamic model

3.1 Kinematics

In order to build a model of the system the kinematic relations need to be determined. Figure 5 describes the definition of the model.

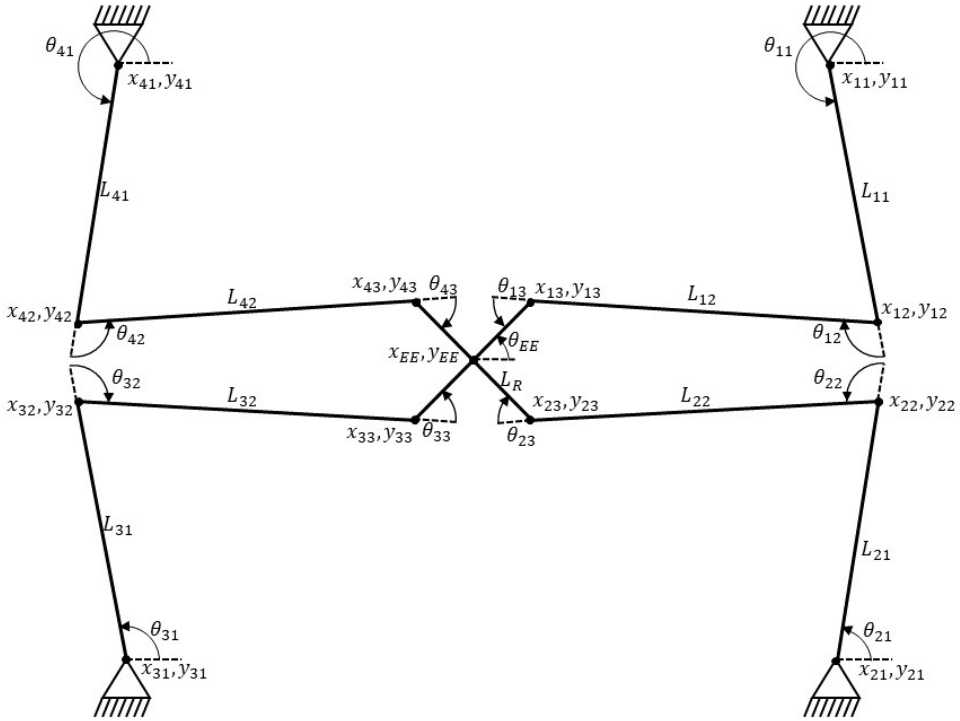

Figure 5: Topology of the system with all coordinates

$$\boldsymbol{q} = [\theta_{EE} \quad x_{EE} \quad y_{EE}]^T \tag{1}$$

The vector $\boldsymbol{q}$ is defined as the independent coordinates as can be seen in equation 1. These coordinates are related to the centre point of the end-effector and express its movement in the DOFs. The centre of the end-effector is also the definition of the origin of the global coordinate system. The end-effector is modelled as a rigid cross where the wrist hinge connects to.

The definition of the forward kinematics is the kinematic relation from the driven input angle of the actuators $\boldsymbol{\theta}_a$ to end-effector motion, where $\boldsymbol{\theta}_a$ is defined as:

$$\boldsymbol{\theta}_a = [\theta_{11}, \theta_{21}, \theta_{31}, \theta_{41}]^T \tag{2}$$

This relation has a redundancy problem which will be discussed later. The inverse kinematics describe the relation from the degrees of freedom to the system to the actuator angles. This problem has a analytic solution.

The system motion of all dependent coordinates will be described using the independent coordinates. To do this a set of geometric transfer function is used [19][20]. Using the geometric transformation equations the relation can be described as follows:

$$\boldsymbol{x} = \boldsymbol{\mathcal{F}}(\boldsymbol{q}) \tag{3}$$

where $\boldsymbol{x}$ contains all generalized coordinates in the system, $\boldsymbol{\mathcal{F}}$ the geometric transfer function and $\boldsymbol{q}$ the independent generalized coordinates. As described previously, all generalized coordinates can be analytically described as function of the independent coordinates. The system has 36 coordinates, therefore $\boldsymbol{\mathcal{F}}$ will be a vector of 36 functions. The following equation describes the deformation coordinates $\boldsymbol{\varepsilon}$:

$$\boldsymbol{\varepsilon} = \boldsymbol{\mathcal{E}}(\boldsymbol{q}) \tag{4}$$

The symbol $\boldsymbol{\mathcal{E}}$ represents geometric transfer function of the deformation coordinates. In case of this system the deformation coordinates are defined as all absolute joint angles angles θ. The system has 12 joints, which are defined as the deformation coordinates, thus $\boldsymbol{\mathcal{E}}$ is a vector consisting of 12 functions. Together $\boldsymbol{\mathcal{F}}$ and $\boldsymbol{\mathcal{E}}$ form the geometric transfer functions of the system. A subset of $\boldsymbol{\mathcal{E}}$ is $\boldsymbol{\mathcal{E}_a}$:

$$\boldsymbol{\theta}_a = \boldsymbol{\mathcal{E}_a}(\boldsymbol{q}) \tag{5}$$

Here only transfer function from the independent coordinates to the actuator angles is included. This relation will be used for actuator redundancy.

The first and second order derivatives of the geometric transfer function are also known as the Jacobian and Hessian respectively. The following equations shows how the Jacobian and Hessian of the transfer function are computed:

$$\boldsymbol{\mathcal{F}}_{,\boldsymbol{q}} = \left[\frac{\partial \boldsymbol{\mathcal{F}}}{\partial\, x_{EE}}, \frac{\partial \boldsymbol{\mathcal{F}}}{\partial\, y_{EE}}, \frac{\partial \boldsymbol{\mathcal{F}}}{\partial\, \theta_{EE}}\right] \tag{6}$$

$$\boldsymbol{\mathcal{F}}_{,\boldsymbol{qq}} = \left[\frac{\partial \boldsymbol{\mathcal{F}}_{,\boldsymbol{q}}}{\partial\, x_{EE}}, \frac{\partial \boldsymbol{\mathcal{F}}_{,\boldsymbol{q}}}{\partial\, y_{EE}}, \frac{\partial \boldsymbol{\mathcal{F}}_{,\boldsymbol{q}}}{\partial\, \theta_{EE}}\right] \tag{7}$$

In this equation the first order geometric transfer function $\boldsymbol{\mathcal{F}}_{,\boldsymbol{q}}$ is the geometric transfer function differentiated for each independent coordinate. The second order geometric transfer function $\boldsymbol{\mathcal{F}}_{,\boldsymbol{qq}}$ uses the first geometric transfer function and is differentiated for each independent coordinate. The Jacobian (first order geometric transferfunction) results in a matrix of size 36x3 and the Hessian (second order geometric tranferfunction) results in a 36x3x3 matrix where each element represents a second partial derivative of a transfer function. The first order geometric transferfunction $\boldsymbol{\mathcal{E}}_{,\boldsymbol{q}}$ is obtained from using:

$$\boldsymbol{\mathcal{E}}_{,\boldsymbol{q}} = \left[\frac{\partial \boldsymbol{\mathcal{E}}}{\partial\, x_{EE}}, \frac{\partial \boldsymbol{\mathcal{E}}}{\partial\, y_{EE}}, \frac{\partial \boldsymbol{\mathcal{E}}}{\partial\, \theta_{EE}}\right] \tag{8}$$

This is the same procedure as for $\boldsymbol{\mathcal{F}}_{,\boldsymbol{q}}$. The matrix $\boldsymbol{\mathcal{E}}_{,\boldsymbol{q}}$ is of size 12x3. The geometric transfer function $\boldsymbol{\mathcal{E}}_a$ represents the actuator angle as a function of the degrees of freedom. $\boldsymbol{\mathcal{E}}_a$ is a 4x1 vector and a subset of $\boldsymbol{\mathcal{E}}$. Its derivative with respect to the degrees of freedom is therefore a matrix of size 4x3.

The geometric transfer function of equation 3 can analytically be determined by using the kinematic relations of the system. The kinematic relations use the definition of the system as given in Figure 5. When modelling the end-effector as a cross, as can be seen in the figure, the following relation can be found.

$$\begin{aligned} x_{13} =& x_{EE} + \cos\left(\theta_{EE} + \frac{\pi}{4}\right) L_R \\ y_{13} =& y_{EE} + \sin\left(\theta_{EE} + \frac{\pi}{4}\right) L_R \end{aligned} \tag{9}$$

This relation describes one of the points of the end-effector. The parameter L_R is half the length of the end-effector square diagonal. The addition of $\frac{\pi}{4}$ is due to the fact that θ_{EE} is an absolute angle and in the neutral configuration the end-effector square coordinate point of x_{13} y_{13} is at an angle of $\frac{\pi}{4}$ rad compared to the global coordinate system. To compute the remaining points of the end-effector square, $\frac{\pi}{2}$ needs to be added to the value of $\frac{\pi}{4}$ rad. Therefore, this equation can be modified to describe the whole end effector square as a function of the end effector coordinates. In order to express the coordinates and angles of each arm in terms of the end-effector the following equation needs to be solved:

$$\begin{aligned} x_{13} &= x_{11} + L_{11}\cos(\theta_{11}) + L_{12}\cos(\theta_{11}+\theta_{12}) \\ y_{13} &= y_{11} + L_{11}\sin(\theta_{11}) + L_{12}\sin(\theta_{11}+\theta_{12}) \end{aligned} \tag{10}$$

Each arm can be seen as a double pendulum. The equation provides the kinematic relation for each arm. These two equations can be used to solve for θ_{11} and θ_{12}, however this leads to two solutions for each angle. One of the solutions for θ_{11} and θ_{12} are:

$$\theta_{11} = 2\,\mathrm{atan}\left(\frac{2\,L_{11}\,y_{13} - 2\,L_{11}\,y_{11} + \sqrt{s\left({L_{11}}^2 + 2\,L_{11}\,L_{12} + {L_{12}}^2 - {x_{11}}^2 + 2\,x_{11}\,x_{13} - {x_{13}}^2 - {y_{11}}^2 + 2\,y_{11}\,y_{13} - {y_{13}}^2\right)}}{{L_{11}}^2 - 2\,L_{11}\,x_{11} + 2\,L_{11}\,x_{13} - {L_{12}}^2 + {x_{11}}^2 - 2\,x_{11}\,x_{13} + {x_{13}}^2 + {y_{11}}^2 - 2\,y_{11}\,y_{13} + {y_{13}}^2}\right) \tag{11}$$

$$\theta_{12} = -2\,\mathrm{atan}\left(\frac{\sqrt{s\left({L_{11}}^2 + 2\,L_{11}\,L_{12} + {L_{12}}^2 - {x_{11}}^2 + 2\,x_{11}\,x_{13} - {x_{13}}^2 - {y_{11}}^2 + 2\,y_{11}\,y_{13} - {y_{13}}^2\right)}}{s}\right) \tag{12}$$

$$s = -{L_{11}}^2 + 2\,L_{11}\,L_{12} - {L_{12}}^2 + {x_{11}}^2 - 2\,x_{11}\,x_{13} + {x_{13}}^2 + {y_{11}}^2 - 2\,y_{11}\,y_{13} + {y_{13}}^2 \tag{13}$$

Equation 13 is used to simplify the solution and make it more readable. There exists one more solution for both angles. This is a result of the fact that a double pendulum can reach the same position (in this case the position of x_{13} and y_{13}) with two different configurations. Due to the configuration of the system as given in section 2.6, both configuration of the double pendulum are used as can be seen in Figure 2b. By combining the solution for θ_{11} and θ_{12} for each arm and the solution for x_{13} and y_{13} for each end-effector point every angle and coordinate can analytically be described as function of the degrees of freedom. These inverse kinematics are used to describe the dynamics of the system. The forward kinematics will be described in section 4.2.

3.2 Dynamics 3 degrees of freedom

The system can dynamically be modelled in order to obtain the equations of motions. This is usefull for simulation in MATLAB SIMULINK to be able to design and tune a controller for the system. In that case the dynamic model is used to be able to test the controller first before using it on the physical system. Another use is to be able to predict the necessary input forces for a given system acceleration. The predicted input forces can be used as a feed-forward controller.

In general the equations of motions can be represented as follows:

$$\overline{\boldsymbol{M}}\ddot{\boldsymbol{q}} + \overline{\mathbf{C}}(\boldsymbol{q}, \dot{\boldsymbol{q}})\dot{\boldsymbol{q}} + \boldsymbol{T_s} = \boldsymbol{T_a} \tag{14}$$

where $\boldsymbol{T_a}$ is the vector with the applied forces. Further information on this vector is given in section 4.1. Each of the remaining components of the equation of motion is defined separately.

The mass matrix of the system is described as a lumped mass matrix formulation, where the mass is located in each coordinated. This results in a 36x36 diagonal mass matrix $\boldsymbol{M}$, which

contains the mass for every coordinate of the system. This includes the mass on the nodes and the inertias of all angles of θ. To obtain the reduced mass matrix the following equation is used:

$$\overline{\boldsymbol{M}} = \mathcal{F}_{,\boldsymbol{q}}^{T} \boldsymbol{M} \mathcal{F}_{,\boldsymbol{q}} \tag{15}$$

where $\mathcal{F}_{,\boldsymbol{q}}$ is the Jacobian of the geometric transfer function and $\boldsymbol{M}$ the mass matrix. The reduced mass matrix is a matrix of size 3x3. The velocity dependent inertia terms, also known as the Coriolis matrix, is determined using the following equation:

$$\overline{\mathbf{C}}(\boldsymbol{q}, \dot{\boldsymbol{q}}) = \boldsymbol{\mathcal{F}}_{,\boldsymbol{q}}^{T} \left(\boldsymbol{M} \boldsymbol{\mathcal{F}}_{,\boldsymbol{qq}} \right) \dot{\boldsymbol{q}} \tag{16}$$

In this equation the lumped mass matrix is used together with the transpose of the Jacobian and the Hessian. The stationary forces T_s are determined using:

$$\boldsymbol{T_s} = \boldsymbol{\mathcal{E}}_{,\boldsymbol{q}}^{T} \boldsymbol{K} \boldsymbol{\mathcal{E}} \tag{17}$$

Where $\boldsymbol{K}$ is the constant stiffness matrix of the system with the geometric first order transposed transfer function $\boldsymbol{\mathcal{E}}_{,\boldsymbol{q}}^{T}$ and the geometric transfer function $\boldsymbol{\mathcal{E}}$. The stiffness matrix of the system consist of the rotational stiffness of every joint. This results in a diagonal 12x12 matrix of the system as there are 12 joints. The equation of motion from equation 14 can be rewritten to:

$$\ddot{\boldsymbol{q}} = \left(\bar{\boldsymbol{M}} \right)^{-1} \left(\boldsymbol{T_a} - \boldsymbol{T_s} - \overline{\mathbf{C}}(\boldsymbol{q}, \dot{\boldsymbol{q}}) \dot{\boldsymbol{q}} \right) \tag{18}$$

such that the equation of motion can be used to simulate the system in SIMULINK as the plant.

3.3 Dynamics multi degree of freedom

SPACAR is a software program based on non-linear finite element theory for a multi degree of freedom mechanism. The program is able to analyse the dynamics of planar and spatial mechanisms, including a manipulator with flexure joints [21] [22]. For the optimization process the information about the eigen-frequencies, stresses and reaction forces of the model are used. This information is obtained by evaluating a SPACAR model of the system. The SPACAR model is build by mapping the system in nodes and connecting these nodes with elements. For each element its mechanical properties is defined, by the material and degree of freedom of a node. Optionally each node can be assigned with a force or displacement.

It is important for the SPACAR model that the kinematic relations of the model are modelled correctly and are able to scale with the optimization parameters. One of limitations of the software is that it is not affected by collisions, it will build each model as the nodes and elements are defined. Therefore the model and optimization needs to be formulated such that each combination of optimization variables does yield a feasible model. Another limitation is the maximum number of degrees of freedom and elements in a model. One of the problem that occurs as a result, is the inability to model constrained warping correctly in SPACAR. Constrained warping phenomena is an increase in torsional stiffness of a flexure when both sides of the flexure are clamped and thus cannot warp. The constrained warping property is a function of the aspect ratio of the leaf spring. A short and high flexure has high constrained warping effects. SPACAR can model these constrained warping effects, however it needs to have each leaf spring element divided in 3 beams to reach proper convergence. As the limitation in size model was already reached, no more additional beams could be added. As an alternative an estimation of the additional torsional stiffness due to constrained warping is used. For this assumption the torsional stiffness is multiplied with a dimensionless stiffening factor γ, for which an analytical approximation of the stiffening factor is given in [23]:

$$\gamma = \frac{ic}{ic - 2\tanh(ic/2)} \tag{19}$$

where the aspect ratio $i = L/h$ and the constant $c = \sqrt{24/(1+\nu)}$ are used. The aspect ratio is defined by the length and height of the leaf-spring while the constant c only depends on the Poisson ratio ν.
The final SPACAR limitation is the calculation speed of each simulation. Specifically for optimization purposes the lack of speed in calculations provides a drawback. For each optimization iteration the whole simulation needs to be run again. Currently, a SPACAR simulation takes 8 minutes.

4 Redundancy

The redundancy of the system exists because there are more actuators and sensors than there are degrees of freedom. For actuation, three equations for each degree of freedom need to be solved for four unknown motor torques. For sensing, the problem is reversed where four inputs need to lead to three solutions for the three degrees of freedom.

4.1 Actuator redundancy

The redundant actuation leads to an under-determined system. The position of the end-effector in its three degrees of freedom can be reached with infinite possible combinations of actuator torques. The relation between actuator torques $\boldsymbol{\tau_a}$ and end-effector forces and torque $\boldsymbol{T_a}$ can be found using the Jacobian. The Jacobian $\boldsymbol{\mathcal{E}_{a,q}}$ describes the kinematic relation between the linear and angular velocities of the actuators and the end-effector. It also links the actuator moments to the forces and moment in the end-effector. The formulation of the relation is:

$$\boldsymbol{T_a} = \boldsymbol{\mathcal{E}}_{a,\boldsymbol{q}}^T \boldsymbol{\tau_a} \tag{20}$$

where $\boldsymbol{T_a}$ is a vector with the applied forces in the end-effector in terms of degrees of freedom, obtained from the equation of motion in equation 14. $\boldsymbol{\tau_a}$ is a vector with the four actuator torques. This means that the Jacobian $\boldsymbol{\mathcal{E}}_{a,\boldsymbol{q}}^T$ is a non square matrix. As mentioned before there a multiple solutions for the actuator torque. The best solution for the actuators is to achieve the end-effector forces with the minimum required actuator load. This results in an optimization problem. Applying the algorithm proposed in [24] and applied in [9] an optimal solution can be found with:

$$\boldsymbol{\tau_a} = \left(\boldsymbol{\mathcal{E}}_{a,\boldsymbol{q}}^T\right)^\dagger \boldsymbol{T_a} + \lambda \,\mathrm{null}\left(\boldsymbol{\mathcal{E}}_{a,\boldsymbol{q}}^T\right) \tag{21}$$

In this equation the Moore-Penrose pseudoinverse of the Jacobian $\boldsymbol{\mathcal{E}_{a,q}}$ is used together with the optimization variable λ and the null space solution of $\boldsymbol{\mathcal{E}_{a,q}}$. The unique solution of the Moore-Penrose pseudoinverse is not the most efficient solution. To obtain he most efficient solution, the value for λ is chosen such that the maximum of the four actuator torques is at a minimum. This means that the optimal solution avoids the saturation limit of the actuators as much as possible. This effectively applies the is the $\|H\|_\infty$ norm to equation 21 to obtain the ideal λ value [25].

4.2 Encoder redundancy

Similar to the actuator redundancy, there is encoder redundancy. Because there are four actuators present there are also four encoders. This results in redundant sensing. Each encoder measures the angle of the actuator resulting in the measurement of four actuator angles while the end-effector of the system moves in three degrees of freedom. The method proposed in [9] uses theory from [26]. The goal is to describe the motion of the end-effector in its three degrees of freedom, using the actuator angles measured by the encoders.

The movement of the joints enforces kinematic constraints on the system. The kinematic constraints can be used to solve the system. There are multiple solutions to formulate the kinematic constraints. One of the possibilities is given:

$$\boldsymbol{S}\left(\boldsymbol{q}\right) = \begin{bmatrix} \left(x_{13} - x_{12}\right)^2 + \left(y_{13} - y_{12}\right)^2 - L_{12}^2 \\ \left(x_{23} - x_{22}\right)^2 + \left(y_{23} - y_{22}\right)^2 - L_{22}^2 \\ \left(x_{33} - x_{32}\right)^2 + \left(y_{33} - y_{32}\right)^2 - L_{32}^2 \\ \left(x_{43} - x_{42}\right)^2 + \left(y_{43} - y_{42}\right)^2 - L_{42}^2 \end{bmatrix} \tag{22}$$

Where the position of the wrist $(x_{13,23,33,43}; y_{13,23,33,43})$ is used , with the position of the elbow $(x_{12,22,32,42}; y_{12,22,32,42})$ and the length of the lower arm $(L_{12,22,32,42})$.
$S(\boldsymbol{q})$ describes the constraint function as a function of the degrees of freedom $\boldsymbol{q}$ (see equation 1). The constraint equations coordinates depend on the actuator angles θ_a, as described in equation 2 and are not directly shown in the constraint function. However using forward kinematics in equation 10 each actuator angle directly describes the position of the corresponding elbow hinge. Similarly, the solution of all wrist hinge coordinates is kinematically linked to the end-effector degrees of freedom as can be seen in equation 9. Therefore this set of constrain equations links the actuator angles $\boldsymbol{\theta}_a$ to the independent coordinates $\boldsymbol{q}$. To solve the set of constraint equation the Newton Rapshon method is used [26].

$$\boldsymbol{q}_{i+1} = \boldsymbol{q}_i - [\boldsymbol{S}_{,\mathbf{q}}(\boldsymbol{q}_i)]^{\dagger} \cdot \boldsymbol{S}(\boldsymbol{q}_i) \tag{23}$$

In the equation the new updated step of the Newton Rapshon method $\boldsymbol{q}_{i+1}$ is dependent on the previous step $\boldsymbol{q}_i$ minus the pseudo-inverse of the Jacobian of the constraint equation $([\boldsymbol{S}_{\boldsymbol{q}}(\boldsymbol{q}_i)]^{\dagger})$ times the constraint equation evaluated at the previous step $(\boldsymbol{S}(\boldsymbol{q}_i)$. Because the Newton-raphson method relies on the previous step the start-up of this method uses the initial known configuration of the system. The iterative method results in a more accurate answer at every iteration. However during real time usage there is only limited time to iterate.

5 Control

The motion of the mechanism is controled using a controller. In this chapter a method to design and implement a controller is proposed. In order to test a controller concept and tune the parameters, a controller scheme can be modelled in MATLAB SIMULINK. After the controller design and tuning is done in simulation software, the modelled system can be replaced by the real system.

5.1 Overall controller structure

For this system a PID controller is proposed. In figure 6 the simplified control scheme is shown. This control scheme includes a feedback and feed-forward controller as well as the plant and both actuator redundancy and encoder redundancy.

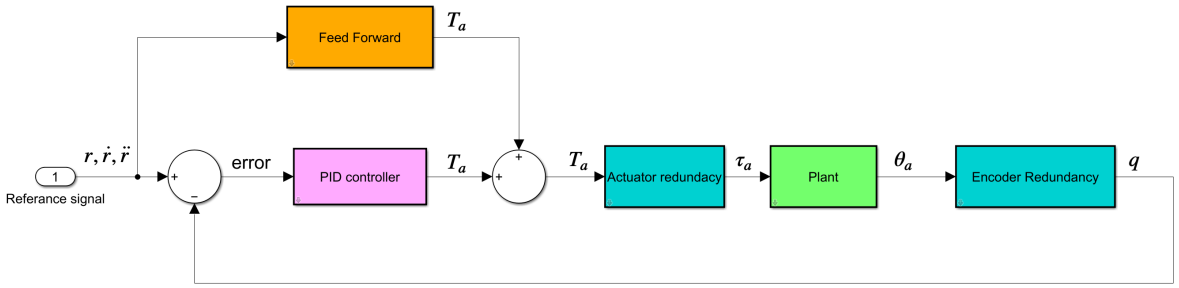

Figure 6: Proposed control scheme

For the simulations in SIMULINK the block that is noted as plant will consist of the equation of motion of the system. The equation for the plant is given in equation 18. The movement of the plant is expressed in its degrees of freedom, however the input torque and measured rotation is done at the actuators. Therefore a block is placed before after the plant, containing the actuator redundancy equations of section 4.1 before the plant and the equations of section 4.2 for the encoder redundancy after the plant. These are visible as the cyan colored blocks. For simulations in SIMULINK the input torques τ_a for the actuators need to be transformed to forces T_a acting on the end-effector. Only then the equation of motion as given in equation 18 can be used to simulate the plant. The relation for the transformation from actuator torques to end-effector forces is given in equation 20. For the physical test setup the figure shows a correct controller scheme.

5.2 Feed-forward Control

The controller performance can significantly increase by including a feed-forward controller. Such a controller is especially suitable for compliant mechanisms due to the lack of unknown parameters such as friction. The equation of motion of the system as given in equation 14 is used to compute the feed-forward controller. This equation needs the trajectory and its related velocity and acceleration of the reference signal as input. The equation of motion computes which forces will act on the end-effector as a result. With a perfect feed-forward controller the equation of motion used in this controller exactly describes the dynamic behaviour of the plant. As a result, the forces from the feed-forward controller will result in perfect tracking of the reference signal. However in practice the calculated equation of motion is never a perfect match with the real world behaviour of the plant. Reason for this is that the feed-forward controller cannot compensate for unknown disturbances and the model can have modelling error and inaccuracies.

The input reference signal $\boldsymbol{r}(t)$ for the feed-forward controller is the desired position of the end-effector and describes the desired position in each degree of freedom. Differentiating the signal to be used in the feed-forward controller: $r(t) = \boldsymbol{q}(t)$ results in $\dot{\boldsymbol{q}}(t)$ and $\ddot{\boldsymbol{q}}(t)$.

5.3 Feedback control

Due to the for mentioned reasons a feedback controller is necessary to be able to have good tracking. To simplify the controller multiple singel input single output (SISO) controller are considered instead of a multiple input multiple output (MIMO) controller. This is only possible if the in and output of the controller can be considered independent and thus the reduced mass matrix of the EOM is assumed diagonal. For this system, the end-effector needs to be controlled in 3 DOF. Therefore, 3 SISO controllers can be used. The assumption can be tested in an experimental setup, if the off-diagonal terms are significantly lower in gain compared to the diagonal for the in and output relation of the system. From previous research on a similar system it was concluded that this assumption holds [9]. Each SISO controller consist of a PID controller with the following transfer function:

$$K_{PID}(s) = k_p \frac{(s\tau_z + 1)(s\tau_i + 1)}{s\tau_i (s\tau_p + 1)} \tag{24}$$

The PID controller is tuned with the parameters k_p, τ_z, τ_i and τ_p. The formulations for each tuning parameter are:

$$\tau_z = \frac{\sqrt{\frac{1}{\alpha}}}{\omega_c} \tag{25}$$

$$\tau_i = \beta \cdot \tau_z \tag{26}$$

$$\tau_p = \frac{1}{\sqrt{\frac{1}{\alpha}} \cdot \omega_c} \tag{27}$$

$$k_p = \frac{m_{eq} \cdot \omega_c^2}{\sqrt{\frac{1}{\alpha}}} \tag{28}$$

These parameters will aid in tuning the PID controller. The parameters in these equations are: α, β, ω_c and m_{eq}. β determines the ratio between τ_i and τ_z and should be chosen larger than 1. The parameter α is typically chosen between 0.1 and 0.3 and is an indicator for the amount of phase lead. m_{eq} is the equivalent mass for each SISO PID controller and can be obtained from the reduced mass matrix. A higher crossover frequency will lead to more bandwidth and allows for faster response. This will come at the expense of stability, as the phase margin is reduced [5]. The crossover frequency is likely limited by the first parasitic eigen frequency. The crossover frequency for the real time control needs to be set after system identification.

6 Optimization

The system design was achieved through an optimization process conducted in MATLAB, using the FMINCON function from the optimization toolbox. FMINCON is specifically designed to minimize a multi-variable objective function while considering both linear and nonlinear constraints. The objective function integrates system properties, such as maximum stress and eigen-frequencies, which are obtained by simulating a detailed system model using the SPACAR software. This approach allows for an efficient and comprehensive exploration of design alternatives, ensuring optimal performance and meeting specific design requirements.

6.1 Variables and model definition

The general model of the system is defined as the design as described in section 2.6. This model is defined to be used for the SPACAR software. A set of variables is added to this model to allow to vary certain parameters, mainly hinge dimensions. These variables are used in the optimization process as optimization variables. Table 3 shows which variables are used.

Table 3: Optimization variables with description and their upper and lower bounds.

Variable	Description	initial value	upper bound	lower bound	unit
L_{links}	length of the arms	0.15	0.16	0.10	m
L_s	leaf-spring length shoulder	0.03	0.05	0.01	m
t_s	leaf-spring thickness shoulder	0.0006	0.001	0.006	m
h_s	leaf-spring height shoulder	0.05	0.06	0.04	m
L_e	leaf-spring length elbow	0.03	0.05	0.01	m
t_e	leaf-spring thickness elbow	0.0006	0.001	0.006	m
h_e	leaf-spring height elbow	0.05	0.06	0.04	m
L_w	leaf-spring length wrist	0.03	0.05	0.01	m
t_w	leaf-spring thickness wrist	0.0006	0.001	0.006	m
h_w	leaf-spring height wrist	0.05	0.06	0.04	m

The number of variables used is a compromise by definition. More variables could in theory create a more optimal system. But this will come with the cost of additional computational time and with each variable introduced the problem becomes less transparent. Therefore to select the variables to be optimized, some assumptions about the system need to be made.

The parameters in the table determine the shape and size of the system. To start with; the length of the links (L_{links}) defines the length of the upper and lower arm, which means that both are the same length. The remaining variables define the flexures. In section 2.3 the dimensions of a butterfly hinge are defined. This means that λ, α_1 and α_2 are a set value and that the hinge size will scale with the variable L. The leaf spring thickness is defined with t and the height of each leaf spring with h. The value for λ is chosen such that no interference occurs between the rigid parts of the hinge. The thickness of the rigid parts of the hinge are chosen such that these perform rigid compared to the leaf spring. This results in a λ value of 1.2 and a rigid body thickness between 2 and 5mm depending on the location. The size of the end-effector scales with the size of the wrist hinges to prevent interference. The dimensions of the links scales with the height of the shoulder hinge. This results in a beam for each link which is the same height as the shoulder hinge. The width is defined as 1/3 of the height to create a rectangular cross section. The stiffness of the links is incorporated in the SPACAR model. To reduce weight in the system the links are made to be rectangular tubes. The assumption is made that 50 % of cross section is empty.

6.2 Cost function

In order to use Fmincon, a objective function or cost function is drafted. The optimization software will try find a value for the variables from table 3 that lead to the minimum value of the cost function. In the cost function the dynamic properties of the system are needed. They will be provided from the SPACAR simulation and the SPACAR model is dependent on the optimization variables.

The cost-function has as goal to maximise the workspace of the system. However the system still needs to fulfill more requirements than only the workspace. The value of the first parasitic eigen frequency needs to be high enough compared to the eigen frequencies in the degree of freedom modes. Another requirement is that the maximum stress in the material cannot exceed the yield stress. The actuators also provide a requirement as they can only provide a finite amount of torque. The maximum available torque may therefore not be exceeded and some amount of headroom is necessary in stationary position to be able to achieve decent accelerations. These requirements can be written as a non-linear constraint in FMINCON. However FMINCON disregards each optimization iteration when a constraint is violated. This creates a problem because at each iteration the SPACAR model needs to be evaluated, which takes a long time. To shorten the computational time, the requirements are written as soft constraints, which means that violating a constraint results in a rapid increase of the cost function value. The cost function is defined with the variable ϕ_{cost}, the optimization algorithm interior point method searches a the set of parameters from Table 3, that will result in the absolute minimum value of ϕ_{cost}, which is defined as:

$$\phi_{cost} = \frac{\exp\left(\frac{M_{max}-M_{opt}}{M_{opt}}\right)}{(\theta_{pos} \cdot L_{pos})^{-1} \ \cdot \ Z_{mode}} + \exp\left(\frac{\sigma - \sigma_{max}}{\sigma_{max}}\right) \tag{29}$$

The cost function is written as such that the main goal is to make a large motion in order to fulfill the requirement of a large workspace. The value of θ_{pos} determines the angle of rotation of the end-effector and L_{pos} determines the translation of the end-effector diagonally across the xy plane. These two parameters also determine in which position the manipulator is evaluated using SPACAR. The other goal is a high out of plane parasitic eigen-frequency. This goal is represented by the parameter Z_{mode} in equation 29. Z_{mode} is the value of the out of plane eigenfrequency in Hertz. The desired out of plane eigen frequency is set to be 10 times higher than the first eigen frequency in the degree of freedom. The position, angle and frequency are all multiplied with each other such that the optimization algorithm will not optimize the system for just one of the goals. Using multiplication, both rotation and translation are promoted in the algorithm.

The soft constraints are written as exponential functions; as soon as a limit is reached the cost function will exponentially increase, therefore soft constraining the function. In equation 29, the two soft-constraints are shown. One of these constraints is equation 30:

$$C_1 = \exp\left(\frac{M_{max} - M_{opt}}{M_{opt}}\right) \tag{30}$$

where M_{max} is the maximum reaction moment in static deformed configuration of the actuators and M_{opt} is the value to which this maximum moment is constrained. This value is chosen to be 50% of the maximum moment of the actuators as is given in Table 2. This constraint is used such that the stiffness in of the hinges in their rotation direction remains low enough. Too much stiffness in this direction would result in a large moment in the actuators, the limit of 50% is chosen to leave headroom to deliver torque for acceleration.

The second soft constraint is defined as:

$$C_2 = \exp\left(\frac{\sigma - \sigma_{max}}{\sigma_{max}}\right) \tag{31}$$

which constrains the maximum stress in the system. The constraint value of the stress is given by the parameter σ_{max} and σ is the maximum stress found in the system for the given deformation. The value of σ_{max} is defined in Table 1 as the tensile strength of Nylon.

Different configurations of the cost function can be used to reach the goal. The cost function is subjected to a certain degree of subjectivity. The choice was made to use multiplication instead of adding up the values for the translation and rotation. This will result in a compromise between both, but multiplying the translation in meters and the rotation in radians makes this compromise subjective. The choice is made to use weighting factors in the cost function in an effort to normalise the parameters. By sampling the SPACAR model, an estimate is made of the expected maximum translation and rotation as well as the maximum moment and frequency of the Z-mode. Each of these parameters received a weighting factor to prevent one of the parameters to dictate the whole optimization process. This is an iterative process as the weighting factors can be improved after multiple optimization runs. At first the weighting factors are used to normalise all parameters in order to have similar numerical value for the position L_{pos}, rotation θ_{pos} and Z_{mode}. The formulation of the soft constrains already results in a normalised parameter. As a result of the iterative improvement, a higher weighting factor is placed on the Z_{mode}. The parameters to optimize in the optimization process are given in Table 3. The initial values for each of the variables is varied randomly such that the absolute minimum for the cost function is found and not a local minimum.

7 Results

In this chapter, the results of the optimization process of the design are presented. From the optimization scheme a single design is obtained. The optimization result is a direct result of the constraints and cost function used. Figure 7 presents the design retrieved from the optimization process.

A total of 5 iterations with different starting values of for the optimization process have been performed. The results presented in this chapter are the result of the iteration that yields the lowest value of the cost function. The assumption has been made that this result is the global minimum. Other iterations point roughly in the same direction. However every iteration is slightly different. This is believed to be caused by the stopping criteria of the *fmincon* function. The optimization process stopped due to the change in variables being smaller than the minimum set step tolerance. This means not an optimality was the cause that lead to termination of the *fmincon* function. However the step-tolerance is 1e-10, thus the difference between the different iteration is very small.

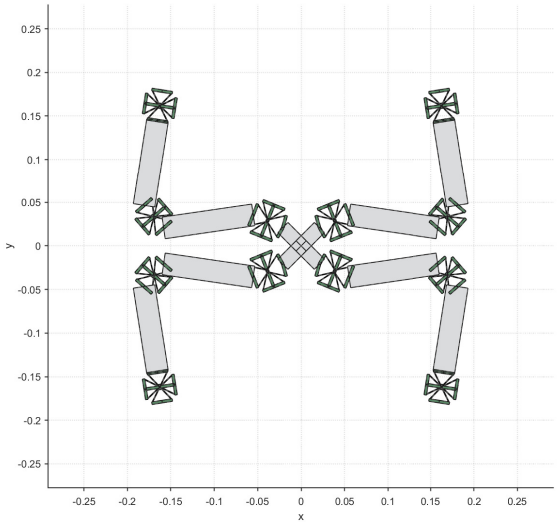

(a) Optimized design from above

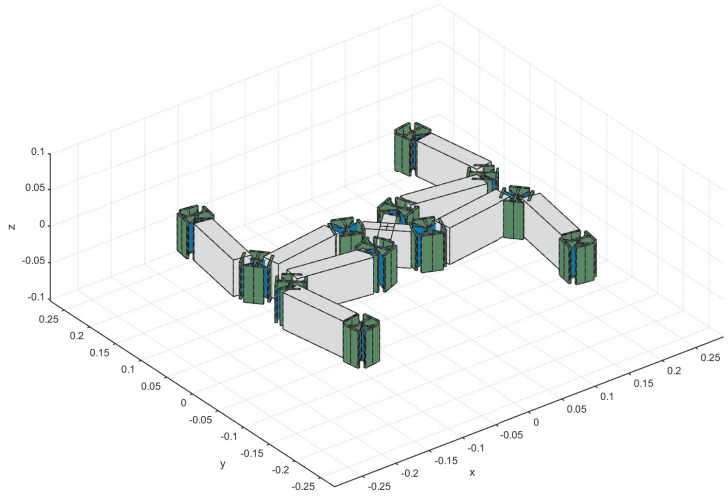

(b) Optimized design 3D

Figure 7: Overview of the result from the optimization process

In Figure 7 the general configuration of the system in undeformed state is visible together with the dimensions of the system. The optimization goal was to maximize the workspace. The maximum deflection found from the optimization process is shown in Figure 8. From the figure it is visible that the movement is a combination of translation in x and y direction with a rotation. The translation found is 41.8 mm in diagonal from the origin, which translates to a 29.55 mm translation in x and y direction. This translation is combined with a rotation of the end effector of 14 degrees. As these values are for the combined movement in each degree of freedom, the movement in for eac degree of freedom individually is different. At this combined deflection, the torque needed to hold that position is 0.15 Nm as maximum. The dashed lines in figure 8 represents the undeformed state and the solid lines represents the deformed state for the given parameters to which the optimization function converged. It is visible that the elbow and wrist hinges receive the most rotational deformation and the shoulder hinge much less. Two of the wrist hinges are for the given deformation at their maximum 30 degree of deflection, two of the elbow hinges stay just below their maximum of 30 degree of rotation. The design of the butterfly hinges defined in section 2.3 dictates that the maximum deformation for each hinge is $\pm$ 30 degrees.

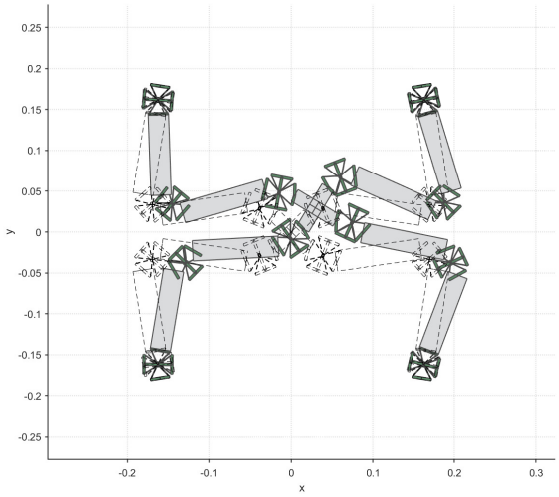

Figure 8: Optimization result deformed state

The minimum for the cost function found in the optimization process is with the values for the parameters as can be seen in Table 4. The minimum found is a compromise between the conflicting goals. One of results shows this compromise clearly. To obtain a large workspace, the length of the arms is desired to be as long as possible, however the length adds weight and therefore has a negative impact on the first parasitic frequency. The found optimum for the arm length is therefore a value that is not constrained by the upper or lower bound but somewhere in the middle.

The length of the different hinges scales from 18.6 mm for the shoulder hinge to 21.4 for the wrist hinge. This corresponds with the shoulder hinge having the least rotation and the wrist hinge having the most rotation. The shoulder hinge is the only hinge were the minimum thickness of the leaf spring is not the optimum solution and a thicker hinge is made. The cause for this result is the relative limit angle of the shoulder and the larger contribution of the shoulder hinge to the support stiffness. This means that the part of the cost function where the out of plane mode is incorporated (Z_{mode}) does affect the design positively and increases the out of plane stiffness. The motion of the first parasitic eigen frequency is shown in Figure 9 and this motion can be

Table 4: Result optimization variables

Variable	Description	value	unit
L_{links}	length of the arms	147.0	mm
L_s	leaf-spring length shoulder	18.9	mm
t_s	leaf-spring thickness shoulder	7.7	mm
h_s	leaf-spring height shoulder	40.3	mm
L_e	leaf-spring length elbow	19.3	mm
t_e	leaf-spring thickness elbow	6.0	mm
h_e	leaf-spring height elbow	41.6	mm
L_w	leaf-spring length wrist	21.4	mm
t_w	leaf-spring thickness wrist	6.0	mm
h_w	leaf-spring height wrist	43.0	mm

described as the out of plane mode. In this figure the mode is shown without deformation in the degrees of freedom.

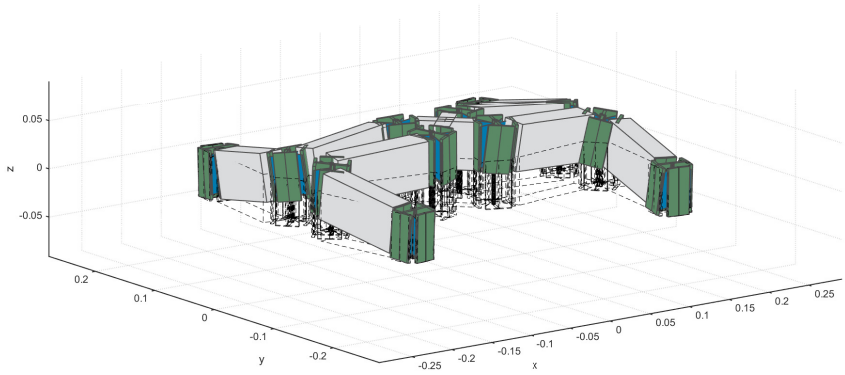

Figure 9: First parasitic eigen-frequency in neutral configuration

The noteworthy eigen-frequencies are noted in Table 5. The difference between undeformed and deformed value for the first parasitic eigen frequency is small. The eigen frequency corresponding to a degree of freedom is most affected when it is also deformed in that direction. In the direction of deformation the eigen frequency becomes larger. The small change of the first parasitic eigen frequency can be contributed to the fact that the shoulder hinge stiffness has the most impact on the out of plane motion. From the optimization process this hinge is made stiffer and smaller. Also its deformation remains the lowest of all hinges. From this table it is also visible that due to the 2 way symmetry of the arm design, the eigen frequencies in x an y are not symmetrical. In Table 5 the eigen frequencies are given for the undeformed state and for the maximum deformation in each separate degree of freedom.

The value of the first parasitic eigen frequency is lower than desired. The goal has been to reach a frequency of 10 times the eigen frequency in the degree of freedom of the system. In the optimization process a higher weighting factor is used to increase the contribution of the first parasitic eigen frequency. However this only resulted in marginal gains and the goal of the first parasitic eigen frequency value was not reached.

Table 5: Result eigen-frequencies

Vibration mode	undeformed	deformed x_{EE}	deformed y_{EE}	deformed θ_{EE}	unit
Translation in x_{EE}	2.213	2.93	2.57	2.27	Hz
Translation in y_{EE}	2.977	3.63	4.28	3.14	Hz
Rotation in θ_{EE}	6.178	6.67	6.62	5.52	Hz
1st Parasitic:	10.94	11.00	11.08	10.74	Hz

The workrange of the end-effector can be limited due to multiple causes. One of the possibilities is interference. This can both be possible between the arms or between hinges or interference in each hinge itself. As noted in section 2.3 the maximum rotational angle of 30 degrees is possible. The interference between components is prevented with the setup of the SPACAR design. Therefore only the interference in the hinge itself is found as a limit. The other possibility for limited workrange is when the maximum stress in a hinge is exceeded.

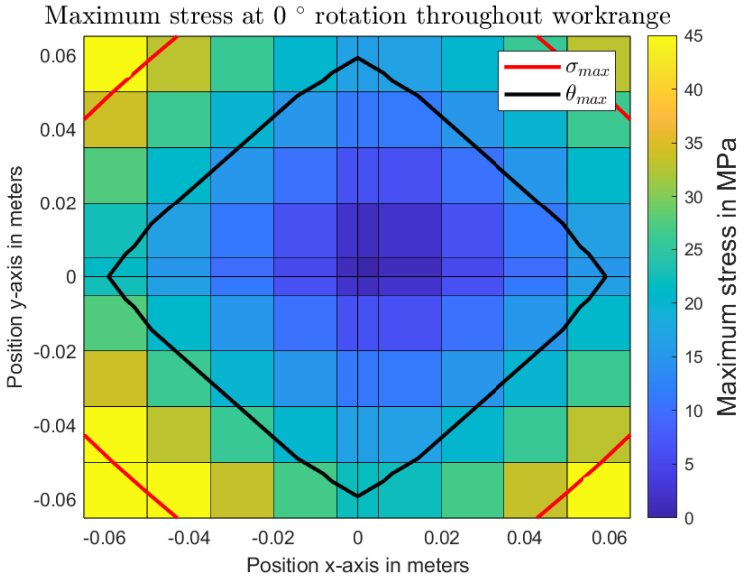

Figure 10: Maximum Stress in the translational working range

The workrange of the design is shown in Figure 10 where only the translation in x and y direction is analysed. The red and black line represent the maximum value of the allowable material stress and the maximum hinge rotation angle respectively. From both these lines it is visible that the work range is not limited by stress, but limited by the rotational capacity of the hinges. The coordinates outside the black contour are in practise not reachable. The black contour line is a result of the combination of the maximum wrist angle and maximum elbow angle.

With no translation movement and only end-effector rotation, a maximum rotation of 27.56 degrees is reached. This maximum angle is limited by the maximum hinge rotation of the wrist of 30 degree. Unlike the pure translation movement, the elbow angle remains significantly below the limit. From Figure 11 it is visible that with pure rotaton the maximum stress (located in the red dot) is lower than the maximum allowable stress of 45 MPa. The exact location of the maximum stress is not visible with the view from above.

When combining translation and rotation, the workspace is reduced compared to pure translation. The maximum allowable wrist and elbow angle are both forming the limit to the maximum range as can be seen in Figure 12. The combination of both determine the maximum workspace,

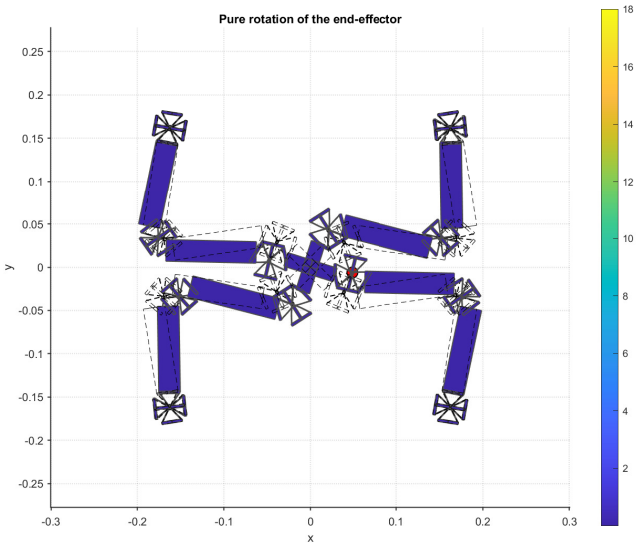

Figure 11: Maximum rotation of the end-effector (no translation)

as can be seen as the black line in the figure. This black line is overlayed on the stress for the same scenario of 15° end-effector rotation. This is visible in Figure 13. Comparing Figure 10 and Figure 13, it can be clearly seen that the translation in x direction does almost not change. This is because the shoulder and elbow joints are responsible for this deformation. The shoulder joint receive little deformation due to the 15° end-effector rotation and from Figure 12 it is visible that the limit in x direction due to the elbow is almost the same as the limit found in Figure 10. Comparing the two figures in y-direction clearly shows a reduced workspace in y direction. Using Figure 12 it can be observed that the wrist joint is responsible for this limitation. The result for -15° rotation is not given; the effect of rotation on the available workspace in each direction is the same due to the 2 way symmetry of the arms.

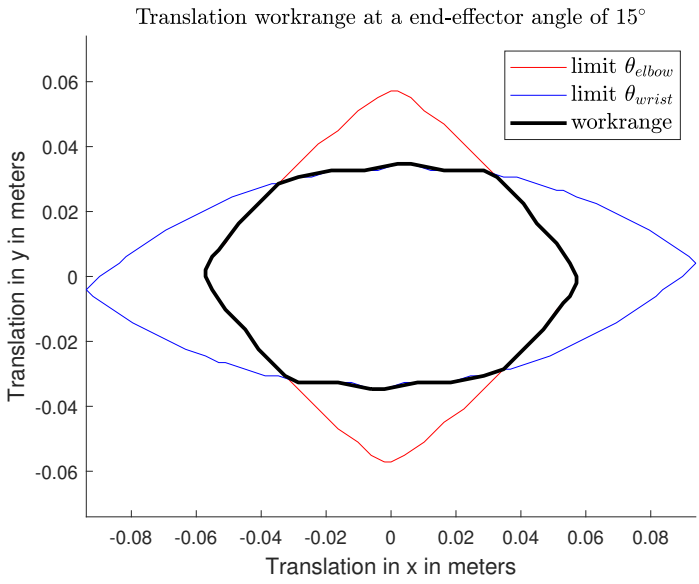

Figure 12: Effect of maximum allowable joint rotation on workspace area

The results of the workspace analysis are summed up in Table 6. As the maximum workspace

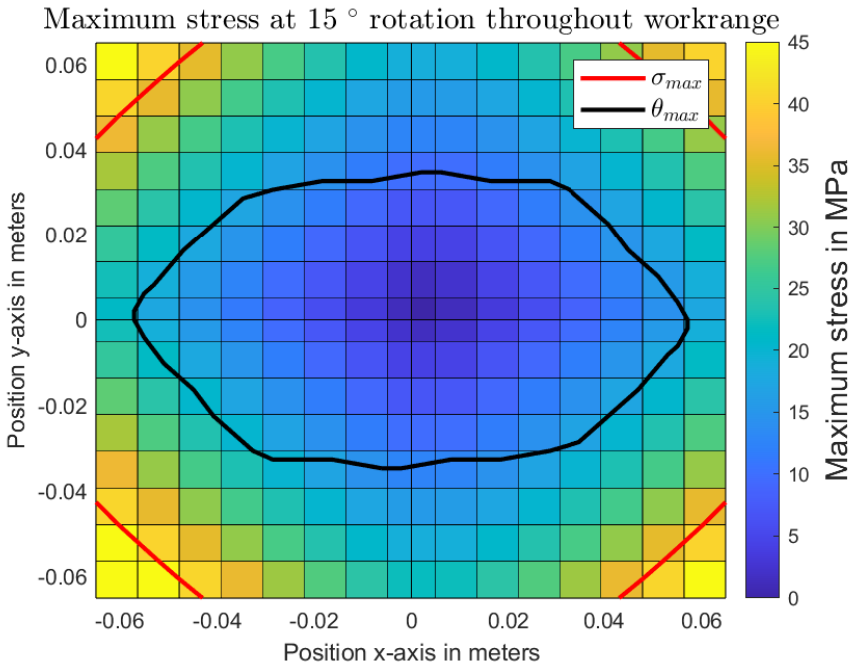

Figure 13: Stress plot of the maximum workrange at 15° end effector rotation

area is defined by maximum joint rotation, the maximum workspace is the area encircled by the black line in both Figure 10 and Figure 13. The maximum workspace can be defined in different ways. Adding rotation will limit the amount of translation. Similarly due to translation the amount of rotation is limited.

Comparing the translational workspace to previous research, the workspace is increased by 3,5

Table 6: Result workrange

Workrange	value	unit	limitation factor
maximum workspace, translation	7772	$[mm^2]$	hinge rotation
maximum rotation, rotation	± 27.5	[°]	hinge rotation
maximum workspace, at 15° rotation	5955	$[mm^2]$	hinge rotation

times [9]. This is achieved while keeping the same position for the actuators, thus the same footprint of the system.

8 Physical model

The physical model uses the design from Chapter 7. Before the implementation to a physical model, some changes need to be made. It is important for the physical model to be as close as possible to the theoretical model in SPACAR. However in the SPACAR model, connectivity is not a issue. This leads to a lack of detail, for example the connection of nodes between different parts are not modelled in SPACAR. Furthermore, interference is completely ignored in SPACAR. For practicality and financial reason each arm and hinge is made as a separate part. The connection between these parts needs to be strong and precise enough while adding the least amount of weight as possible. Figure 14 provides an overview of the Computer Aided Design (CAD) model.

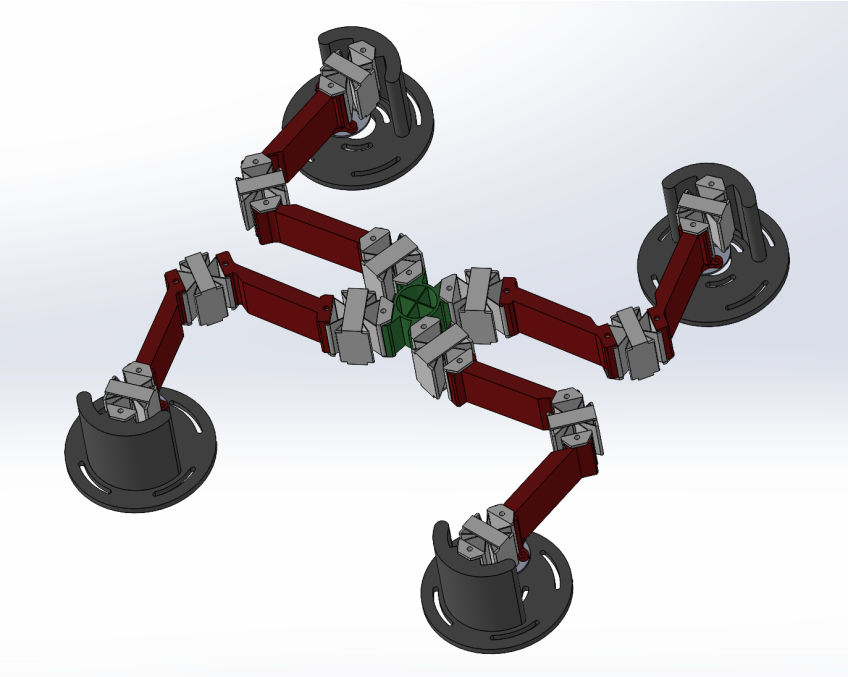

Figure 14: Overview of the CAD model

Each hinge is made from Nylon which allows for a good surface finish and precise dimensions. This allowed to design the connecting elements thinner compared to a PLA part. The intermediary body of the butterfly hinge is a good example where the material can made thinner and therefore lighter than when it would be made from PLA. The connecting mechanism is chosen to be a dovetail joint. This type of joint can be made with good precision and requires only one fastener. The precision of Nylon allows to add small rounded corners at the ends of the leaf spring to prevent high stress concentration.

Each of the arms are made from PLA and have the inverse Dovetail shape to connect to the hinges as can be seen in figure 15. This part has tolerance for the dove tail joint build in to prevent a too tight fit. As mentioned in 6.1 the arms are modelled as tubes with 50% of the area empty. Therefore the arm is build as a rectangular tube with a wall thickness of 2.5mm. However this leads to some weak spots in the arm due to the lack of consistency in the 3D printing process. The upper arm has a connection for the torque plate. The motor is located directly below the pivot point of the shoulder hinge and connected via the torque plate to the upper arm. Shoulder joints are connected to the base plate using a PLA part. This connection to the shoulder also uses the dovetail joint design, the connection to the base plate is done with fasteners. The end effector size is determined from the optimization result. The end effector

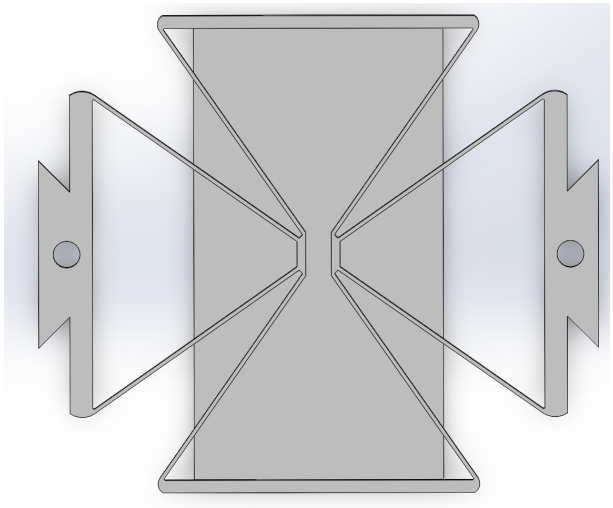

Figure 15: Detail of the elbow hinge

itself is made as a circle to minimize the use of material. The centre cross in the end effector is not structural, but only there to be able to visually track the movement of the end effector better. A detailed image of the end effector is visible in Figure 16.

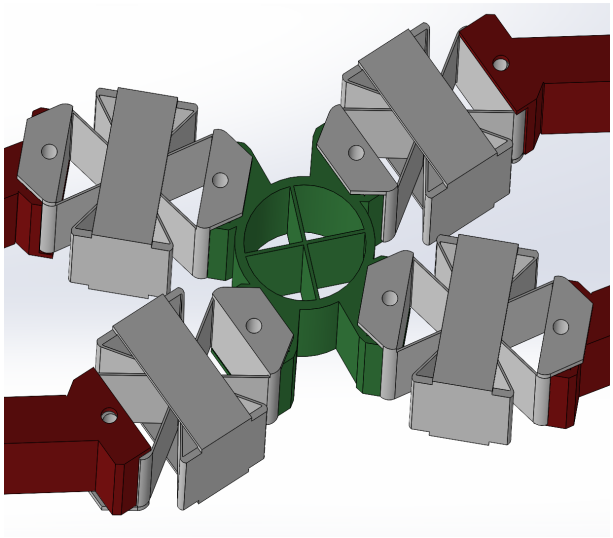

Figure 16: Detail of the end effector

From the physical parts, it can be learned that the arms and end effector are easier to design for light weight compared to the joints. The material density of PLA is not better but it was estimated that these components need less fill rate for the solid material, while the joints made from nylon were estimated to need strong connections for the leafspring to attach to. As a result the end-effector and each arm weigh 19 and 22 grams respectively. Each wrist joint weighs 25 grams despite its equal size footprint. The weight of the end-effector and wrist have the most effect on the first parasitic eigen frequency. The total weight of the end-effector plus wrist joints is 120 grams.

9 Discussion

This study focused on enlarging the available workspace compared to previous design. With the same footprint the workspace reached 3.5 times the area of the previous iteration. The goal was to maintain favorable dynamic properties of the system. However in this department the design falls short. The goal was to achieve a first parasitic eigen frequency that would be 10 times higher than the eigen frequency in the degree of freedom of the system. This would result in a more difficult to control system. Comparing to previous work, the stiffness of the arms and connecting elements in the hinges is incorporated in the model in this study. This could be a possible explanation for the lower than desired first parasitic frequency.

The first parasitic frequency shows little change from undeformed to deformed state. This indicates that the support stiffness in the hinges is not falling off during deformation. The shoulder hinge is mostly responsible for the value of this frequency and with the design as presented the deformation of this joint does not reach the limits of $\pm 30°$. The elbow and wrist joints that do reach this limit have less of an impact on the parasitic eigen frequency. The cost function designed the shoulder hinge as the shortest and thickest hinge, which means that despite the dynamic behaviour of the system not reaching the desired values, the components in the cost function did in fact worked as intended.

The workspace optimization is limited to the maximum angular rotation and not the maximum stress. Therefore the constraint imposed for the maximum stress in the cost function did not have an effect on the design. The constraint on the maximum moment however did. With headroom available in stress, the leaf springs would be made thicker and shorter to achieve a higher parasitic frequency following the goals of the cost function. However, the constraint of the maximum allowable moment caused by the maximum motor torque inhibits this.

The design choice of the two way symmetry resulted from the first simulations results that the stress is lower for the same given displacement as compared to a 4 way symmetry design. With ever other system dimension the same, this means that the joint angle for the same displacement is less. However the 2 way symmetry as chosen, leads to a limit on the arm length due to interference at the location of the elbow joints. The disadvantage of more stress at a given displacement for the 4 way symmetry design could be offset with an increase in arm length.

10 Conclusion

This research has focused on the redesign of the redundantly actuated 3 DOF planar manipulator with flexure joints of [9]. The goal of the research has been to increase the working range of the manipulator. However the design of a flexible manipulator will inevitably lead to a compromise as the design for optimal dynamic properties leads to a different design as when the only focus is on increasing range. In this study both goals are incorporated in an optimization process to find an optimal compromise.

Certain design choices, such as topology of the system and type of joint used, determine the characteristics of the system. The resulting topology and hinge design is focused on achieving large joint deformations with low stress and adequate stiffness properties. Using an optimization process the dimensions of the system are determined. The optimization process is defined by the cost function and the imposed constraints. The cost function is carefully drafted to describe the design compromise. It is important to note that a certain degree of subjectivity is always present in a multi objective optimization process. The optimization results provide a design which results in a maximum workspace in x and y direction of $7772mm^2$ and a pure rotation of the end-effector of $\pm 27.5°$. Both of these values are limited due to the hinge design of the chosen butterfly hinge, which has a maximum rotation $\pm 30°$. The design is successful in achieving the full $\pm 30°$ hinge rotation without contact between parts. The eigen frequencies of the system are 2.2 Hz, 3.0 Hz and 6.1 Hz for the degrees of freedom in x,y and rotation θ direction. The first parasitic eigen frequency is the out off plane vibration of the system and has a frequency of 10.9 Hz.

The goal of the research is achieved by significantly improving the range of motion of the manipulator compared to previous research. However, the dynamic behaviour has deteriorated. The experimental data of the dynamic properties of the manipulator need to be mapped out in further research.

11 Recommendations

The study answered the research question on the redesign of a flexible manipulator for more workspace. However there are still some points that warrant further research. The first and foremost research topic is the experimental system identification and implementation of the proposed controller, in order to put the theory in practise. The goal is to implement the optimized design as faithfully as possible in a experimental model, however this is impossible to fully achieve because a simulation model is a simplification of reality. The experimental results can be used to check how much the physical model deviates from the SPACAR model. The translation from the optimized SPACAR design to a 3D CAD model adds a number of changes to the system.

From the results it appeared that the maximum work space is not limited by the stress of the system but by the maximum possible deformation angle in each hinge. Both the elbow and wrist hinge suffer from this limitation. A larger workspace could be achieved by adding length in the arms or enlarging the rotational deformation of a hinge. A larger arm could be more efficient with a different topology, because with the 2 way symmetry design the arm length is limited due to interference between parts. The 4 way symmetry setup does not have this limitation. The current design of butterfly hinge has a maximum rotation of $\pm 30°$. A redesign of this butterfly hinge or use of a different hing design altogether can be considered. The problem that may arise, is the decrease in support stiffness as the deflection increases. Further optimization in these fields is possible.

The design can further be improved by adding pre-tension to each hinge. The theory of pre-tension reduces effective stiffness of the mechanism in its degree of freedom direction and will therefore lower the needed torques to move the system [27]. When implementing this theory correctly, it is possible to use shorter and thus stiffer hinges that result in the same stiffness in degrees of freedom of the system, but provide an increase in the out off plane stiffness. This therefore, allows for better dynamic performance whilst being able to maintain the same workspace.

References

[1] R. Cornelissen, A. Müller, and R. Aarts, "A compliant and redundantly actuated 2-dof 3rrr pkm: Best of both worlds?," vol. 53, Springer, 2020, pp. 163–171. DOI: 10.1007/978-3-030-23132-3_20.

[2] H. Soemers, *Design principles for precision mechanisms*. Netherlands: University of Twente, 2010, ISBN: 978-90-365-3103-0.

[3] H. Cheng, G. Liu, Y. Yiu, Z. Xiong, and Z. Li, "Advantages and dynamics of parallel manipulators with redundant actuation," in *International Conference on Intelligent Robots and Systems*, 2001.

[4] M. Nahon and J. Angeles, "Force optimization in redundantly-actuated closed kinematic chains," in *Proceedings, 1989 International Conference on Robotics and Automation*, 1989, 951–956 vol.2. DOI: 10.1109/ROBOT.1989.100103.

[5] R. Aarts and J. van Dijk, *Design and Control of Mechatronic Systems (part 2)*. University of Twente, 2017, Lecture notes.

[6] M. Yang, C. Zhang, H. Yu, X. Huang, G. Yang, and Z. Fang, "Kinetostatic modeling of redundantly actuated planar compliant parallel mechanism," vol. 11740 LNAI, Springer Verlag, 2019, pp. 358–369. DOI: 10.1007/978-3-030-27526-6_31.

[7] D. Berendsen, "2dof planar redundantly actuated parallel kinematic manipulator with flexure joints optimization and control," M.S. thesis, University of Twente, 2021.

[8] A. Sridhar and H. Köro͡, "Workspace optimisation and motion control of a redundant flexural 2-dof 3rrr parallel kinematic manipulator," M.S. thesis, University of Twente, 2020.

[9] P. J. A. Stoffels, "Optimization and control of a redundantly actuated 3-dof planar manipulator with flexure joints," M.S. thesis, University of Twente, 2021.

[10] D. Berendsen, A. Sridhar, and R. Aarts, "A compliant and redundantly actuated 2-dof 3rrr pkm: Less is more," in *Proceedings of the10th ECCOMAS Thematic Conference on Multibody Dynamics*, Budapest University of Technology and Economics, 2021, pp. 246–256.

[11] R. Kurtz and V. Hayward, "Multiple-goal kinematic optimization of a parallel spherical mechanism with actuator redundancy," *IEEE Transactions on Robotics and Automation*, vol. 8, no. 5, pp. 644–651, 1992. DOI: 10.1109/70.163788.

[12] P. Buttolo and B. Hannaford, "Advantages of actuatino redundancy for the design of haptic displays buttolo," in *Fourth Annual Symposium on Haptic Interfaces for Virtual Environmentand Teleoperator Systems*, ASME, vol. 57-2, 1995.

[13] S. Kock and W. Schumacher, "A parallel x-y manipulator with actuation redundancy for high-speed and active-stiffness applications," in *International Conference on Robotics and Automation*, 1998.

[14] B. Xu, T. Li, X. Liu, and J. Wu, "Workspace analysis of the 4rrr planar parallel manipulator with actuation redundancy *," 2010.

[15] J. A. Haringx, "The cross-spring pivot as a constructional element," *Flow, Turbulence and Combustion*, no. 313, 1949.

[16] W. Wittrick, "The theory of symmetrical crossed flexure pivots," *Australian Journal of Chemistry*, vol. 1, p. 121, 2 1948. DOI: 10.1071/ch9480121c.

[17] S. Henein, P. Spanoudakis, S. Droz, L. I. Myklebust, and E. Onillon, "Flexure pivot for aerospace mechanisms," 2007.

[18] M. Naves, M. Nijenhuis, W. B. Hakvoort, and D. M. Brouwer, "Flexure-based 60 degrees stroke actuator suspension for a high torque iron core motor," *Precision Engineering*, vol. 63, pp. 105–114, May 2020, ISSN: 01416359. DOI: 10.1016/j.precisioneng.2020.02.001.

[19] J. Jonker, R. Aarts, and J. Meijaard, *Flexible multibody dynamics for design purposes, A Finite Element Approach*. University of Twente, 2020, Lecture notes.

[20] K. Krajoski, A. Müller, H. Gattringer, and M. Jörgl, "Design, modeling and control of an experimental redundantly actuated parallel platform *," in *OAGM and ARW Joint Workshop*, 2016. DOI: 10.3217/978-3-85125-528-7-29.

[21] J. B. Jonker and J. P. Meijaard, "Spacar - computer program for dynamic analysis of flexible spatial mechanisms and manipulators," in *Multibody Systems Handbook*, W. Schiehlen, Ed. Berlin, Heidelberg: Springer Berlin Heidelberg, 1990, pp. 123–143. DOI: 10.1007/978-3-642-50995-7_9.

[22] R. G. K. M. Aarts, J. P. Meijaard, and J. B. Jonker, *Spacar user manual*, User Manual, University of Twente, 2011.

[23] D. H. Wiersma, S. E. Boer, R. G. Aarts, and D. M. Brouwer, "Design and performance optimization of large stroke spatial flexures," *Journal of Computational and Nonlinear Dynamics*, vol. 9, 1 2014, ISSN: 15551415. DOI: 10.1115/1.4025669.

[24] J. H. Choi, T. Seo, and J. W. Lee, "Torque distribution optimization of redundantly actuated planar parallel mechanisms based on a null-space solution," *Robotica*, vol. 32, pp. 1125–1134, 7 2014, ISSN: 14698668. DOI: 10.1017/S0263574713001288.

[25] S. H. Woo, S. M. Kim, M. G. Kim, B. J. Yi, and W. Kim, "Torque-balancing algorithm for the redundantly actuated parallel mechanism," *Mechatronics*, vol. 42, pp. 41–51, Apr. 2017, ISSN: 09574158. DOI: 10.1016/j.mechatronics.2017.01.002.

[26] J. Schilder, *Flexible Multibody Dynamics*. University of Twente, 2020, Lecture notes.

[27] B. G. T. Hoppenreijs, "Static balancing of compliant mechanisms with spiral torsion springs," Bsc thesis, University of Twente, 2022.

A Simulations for topology variations

The used topology is explained in section 2.6. In order to make a choice between the different topology options, multiple simulations have been conducted. The first comparison, is the two way symmetry design to a 4 way symmetry design. All hinges are the same as well as arm length and actuator position. It is important to note that the actuators are positioned as a square. This allows for the best comparison between different arm configurations.

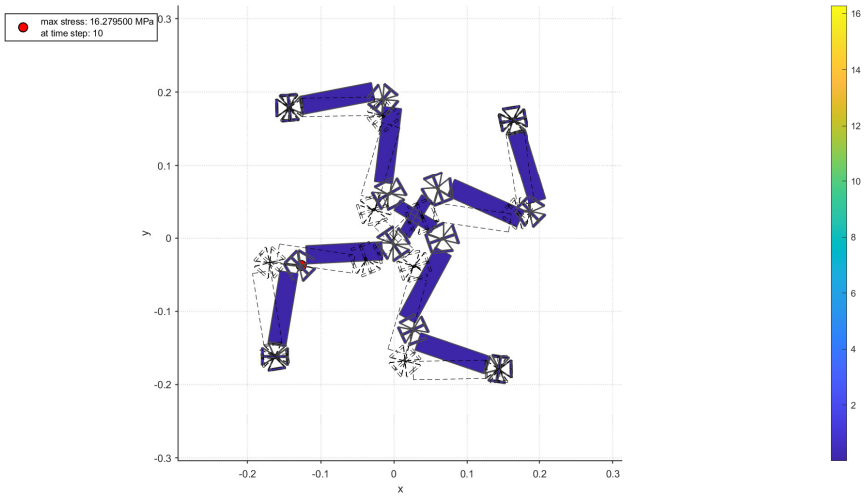

(a) Configuration 4 way symmetry deformed

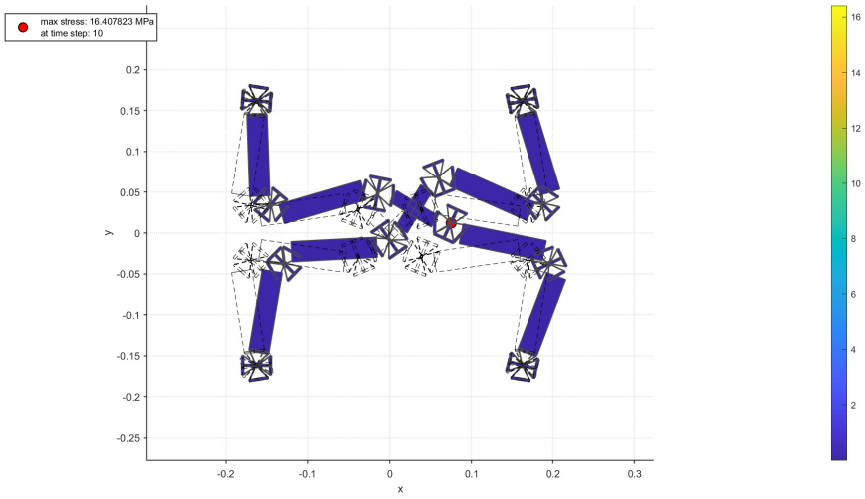

(b) Configuration 2 way symmetry deformed

Figure A.1: SPACAR simulations of both possible arm configurations

Figure A.1 shows the result of both configuration with the same given displacement. The displacement used, is a diagonal translation across the xy plane with an added rotation. This means that all degrees of freedom are used. The figures show that the stress only differs 0.13 MPa between the two configurations. However, stress is not the governing factor, but maximum hinge deformation angle and first parasitic eigen frequency is. The hinge deformation in the wrist is identical, leading to a identical work range for the rotational degree of freedom. However the combination of lower elbow and shoulder hinge rotation for a given position, lead to a larger

available workspace of the 2 way symmetry compared to 4 way symmetry design. The first parasitic frequency, the out off plane mode, is for the 4 way symmetry 10.82 Hz and 10.94 for the for 2 way symmetry. This is a very minor difference in the advantage of the 2 way symmetry topology.

The configuration of the actuators can be altered to a non-square design. Figure A.2 shows

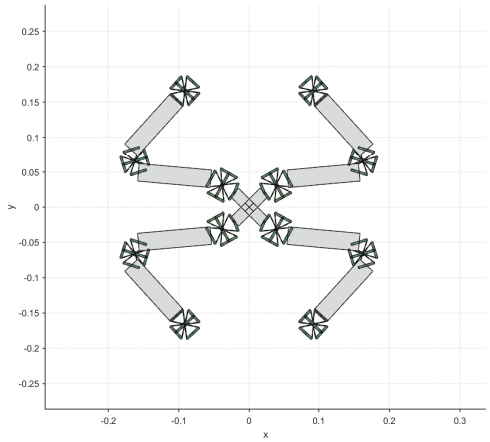

(a) Non square configuration

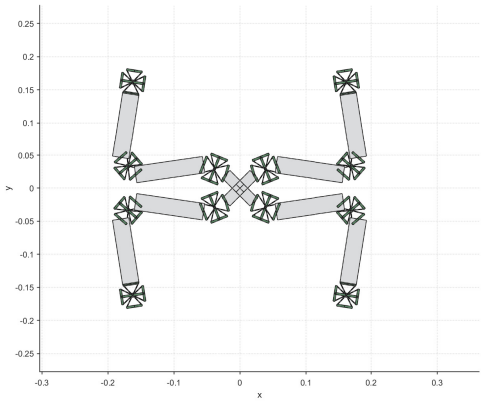

(b) Square Configuration

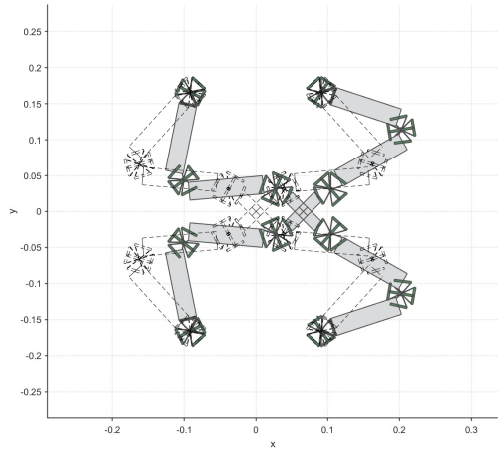

(c) Non square configuration deformed in y-direction

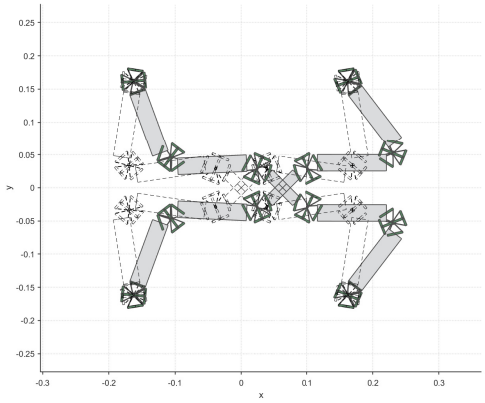

(d) Square Configuration deformed in y-direction

Figure A.2: SPACAR simulations of arm base positions

both cases in undeformed and deformed state. Both configurations are exactly the same except for the actuator configuration. For the simulations the actuator is moved in y direction as this is the direction that is expected to be compromised in the non-square design. From the simulations the decrease in first parasitic frequency from the neutral position to maximum deformation in y direction is -0.5% for the square situation. This means that the first parasitic frequency became slightly higher compared to the neutral position. For the non-square situation the frequency of the out of plane mode decreased with 6.2 % compared to the neutral configuration. This drop-off in frequency in deformed stated can be contributed to the fact that for the same end effector movement, the shoulder hinge in the non-square model needs to deform more compared to the square configuration. The larger deformation leads to a larger decrease in out of plane stiffness for the shoulder hinge compared to the square design. Concluding, the square configuration allows for better out of plane stiffness throughout the work range of the end-effector.